Embedded Cavity Drag in Steady Laminar Flow

T. B. Gatski*
NASA Langley Research Center, Hampton, Virginia
and
C. E. Grosch†
Old Dominion University, Norfolk, Virginia
and
Institute for Computer Applications in Science and Engineering, Hampton, Virginia

The numerical solution of the laminar boundary-layer flow over an embedded cavity is studied. The purpose of the study is to examine the relevant drag characteristics of laminar cavity flow. The solution field is obtained in terms of velocity and vorticity variables, with the stream function and pressure derivable from the directly computed variables. An analysis and comparison is made among four square cavities, ranging in size from 0.25 to 1.00 boundary-layer thickness deep. The dominant flow features are examined in the vicinity of the cavity by means of the stream function and isovorticity contours. The dominant physics in the overall drag characteristics of the flow are examined by an analysis of the pressure and wall shear-stress distributions in the cavity, and upstream and downstream of the cavity. Pressure forces and frictional forces in, and in the vicinity of, the cavity are determined. Stress relaxation distances, both upstream and downstream of the cavity, are calculated and analyzed. The dynamics of the boundary-layer flow over an embedded cavity are summarized. Finally, the relevance of the present results to the control of flow separation in such flows is discussed.

Nomenclature

B	= coefficient matrix used in numerical solver
C_D	= drag coefficient, ≡ total drag/$\frac{1}{2}\rho U_\infty^2$
C_F	= friction coefficient, ≡ friction drag/$\frac{1}{2}\rho U_\infty^2$
C_P	= pressure coefficient, ≡ pressure drag/$\frac{1}{2}\rho U_\infty^2$
d	= nondimensional depth of cavity
ℓ	= nondimensional length of cavity
M	= number of computational grid cells in a particular direction
R	= flow Reynolds number, $= U_\infty \delta_0/\nu$
$R_1(\ ), R_2(\ )$	= residuals used in solution accuracy checks of velocity solver
t	= nondimensional time
u	= nondimensional streamwise velocity, $= \partial\Psi/\partial y$
U_∞	= dimensional freestream velocity; velocity scale used in nondimensionalization
v	= nondimensional normal velocity, $= \partial\Psi/\partial x$
x	= nondimensional streamwise coordinate
y	= nondimensional normal coordinate
δ_0	= inflow boundary-layer thickness, length scale used in nondimensionalization
δ_x, δ_y	= central finite difference operators
ζ	= nondimensional vorticity
Λ	= aspect ratio of computational cell, $\Delta y/\Delta x$
λ_x, λ_y	= discretization ratios; $\lambda_x = \Delta t/\Delta x$, $\lambda_y = \Delta t/\Delta y$
μ_x, μ_y	= finite difference averaging operator
ν	= kinematic viscosity
ρ	= density
τ_w	= nondimensional wall shear stress
ϕ	= nondimensional dependent variable, $= \partial\zeta/\partial x$
Ψ	= stream function
ψ	= nondimensional dependent variable, $= \partial\zeta/\partial y$
Δ_x, Δ_y	= computational grid spacing in the streamwise and normal directions, respectively
∇_x, ∇_y	= backward finite difference operators

Received Dec. 22, 1983; presented as Paper 84-0436 at the AIAA 22nd Aerospace Sciences Meeting, Reno, Nev., Jan. 9-12, 1984; revision received Oct. 3, 1984. This paper is declared a work of the U.S. Government and therefore is in the public domain.

*Research Scientist, Viscous Flow Branch, High-Speed Aerodynamics Division.

†Professor of Oceanography and Computer Science.

I. Introduction

A DISTRIBUTION of roughness elements along an otherwise smooth wall bounding surface can significantly alter the dynamic processes of the flow. In laminar flows, which are relatively stable, such alterations cause little or no change in the surface drag along these surfaces. In turbulent flows, such alterations, in general, cause a surface drag increase; although certain distributions, e.g., longitudinal grooves,[1] have been found to decrease the surface drag. It is, of course, necessary to understand the dynamic mechanisms of such surface flows, both laminar and turbulent, so that effective drag controlling measures can be implemented. In the turbulent case, the flow-surface interaction is rather complex due to the broad spectrum of dynamically relevant scales of motion present in the flow. Initially, it is advantageous to treat a more tractable flow situation which incorporates the important parameters and features of the flow. The two-dimensional laminar boundary-layer flow over an embedded cavity constitutes such an initial approximation, and the purpose of this study is to gain further insight into the dynamics of such flows.

There have been several experimental studies of boundary-layer flows over embedded cavities (e.g., Refs. 2-7). Several of these studies, which were mostly for turbulent boundary-layer flows, concentrated on the overall features of the flow, such as velocity and surface pressure distributions, as well as skin friction variations; other studies concentrated on more dynamic features of the flow, such as interfacial stability characteristics. There have also been numerical studies on the shear flow driven cavity problem (e.g., Refs. 8 and 9). These numerical studies have been limited to high-speed flows and do not provide the insight required in the present case. The intent here is to provide flow characteristic information over a range of cavity sizes in a relatively low-speed near-wall environment, which is typical of the local conditions for roughness elements.

The numerical algorithm is a compact difference scheme expressed in terms of the vorticity and velocity.[10] This work and that appearing in Ref. 11 are applications of the algorithm development presented in Ref. 10 and serve as verification and extensions of the method while also aiding the understanding of the flow dynamics. The compact nature of the algorithm allows for unequally sized computational cells to be easily placed in regions where high resolution is necessary. This aspect of the formulation is important, especially when shear stress and wall-pressure distributions are required. Another important feature of the algorithm is the fact that the dependent variables used in the calculations are interpreted as average values over each edge of the cell. Since these variables are defined at the center of each edge, the corner problem at the upstream and downstream sides of the cavity can be handled in an unambiguous manner. Thus, the pressure induced forces on the vertical walls of the cavity, which are critical in the overall drag characteristics, are accurately computed. Finally, wall shear-stress, or friction velocity, values are extracted easily from the computed results, as well as other derivable flow variables such as stream function. In addition, velocity profiles and vorticity contour maps in the vicinity of the cavity can be generated to allow for a detailed study of the flow dynamics. The present paper discusses the physical characteristics of the flow in the vicinity of the cavity. Dominant flow features are identified along with a discussion of the possible application of such flow embedded cavities to the control and delay of flow separation.

II. Mathematical and Numerical Formulation

The problem considered is the incompressible two-dimensional laminar boundary-layer flow over an embedded cavity (see Fig. 1). The governing differential equations for this flow can be written in terms of the velocity and vorticity as

$$\frac{\partial u}{\partial x}+\frac{\partial v}{\partial y}=0 \tag{1}$$

$$\frac{\partial v}{\partial x}-\frac{\partial u}{\partial y}=\zeta \tag{2}$$

$$\frac{\partial \zeta}{\partial t}+u\frac{\partial \zeta}{\partial x}+v\frac{\partial \zeta}{\partial y}=\frac{1}{R}\nabla^2\zeta \tag{3}$$

where u and v are the nondimensional streamwise and normal velocity components, respectively; ζ the nondimensional vorticity; and $R=U_\infty\delta_0/\nu$ the Reynolds number based on the freestream velocity U_∞ and a reference boundary-layer thickness δ_0. In most previous numerical approaches, the vorticity transport equation is numerically solved in conjunction with an equivalent stream function representation of Eqs. (1) and (2). Such a stream function, vorticity solution field then allows for the calculation of the equivalent velocity and pressure fields. In the present paper, the differential forms, Eqs. (1-3), are discretized directly and, thus, provide a velocity-vorticity description of the flow. Since the details of the discretization and the algorithm appear in Ref. 10, we only present the discretized form of the equations, for completeness, and the various extensions and enhancements unique to the present problem.

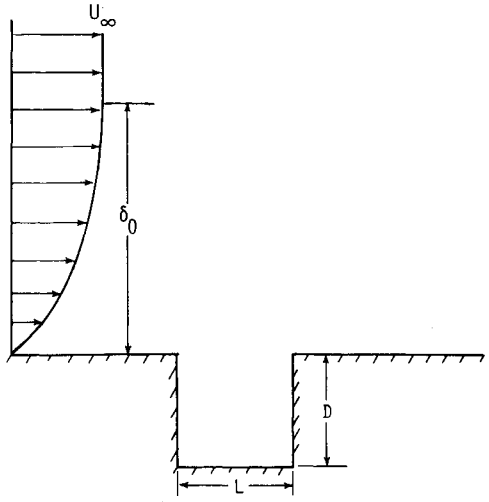

Fig. 1 Cavity embedded in laminar boundary-layer flow.

Since the present formulation can be expressed in Cartesian coordinates, consider the computational cell depicted in Fig. 2 with the associated distribution of dependent variables about the cell. As mentioned earlier, a variable associated with the side of a cell is interpreted as the average of that variable over the side of the cell and one associated with the center of a cell is an average over the cell. In addition, the notation

$$\mu_x w^n_{j,k}=(w^n_{j+\frac{1}{2},k}+w^n_{j-\frac{1}{2},k})/2$$

$$\delta_x w^n_{j,k}=(w^n_{j+\frac{1}{2},k}-w^n_{j-\frac{1}{2},k})/\Delta x_j$$

$$\nabla_x w^n_{j,k}=2(w^n_{j,k}-w^n_{j-1,k})/(\Delta x_j+\Delta x_{j-1}) \tag{4}$$

is used for the x direction in the following; with a completely analogous form used for the y direction. Also, for brevity and to avoid confusion, the spatial indexes will be suppressed, that is, $w^n_{\cdot}=w(\Delta x_j,\Delta y_k,n\Delta t)$. In the following subsections, the velocity and vorticity solvers will be described along with the details of the solution procedure.

A. Velocity Difference Equations and Solver

The difference approximations to Eqs. (1) and (2) and the auxiliary averaging conditions needed in the solution procedure are given by[10]

$$\delta_x u^n_{\cdot}+\delta_y v^n_{\cdot}=0 \tag{5a}$$

$$\delta_x v^n_{\cdot}-\delta_y u^n_{\cdot}=\zeta^{n-\frac{1}{2}}_{\cdot} \tag{5b}$$

$$(\mu_x-\mu_y)u^n_{\cdot}=0, \qquad (\mu_x-\mu_y)v^n_{\cdot}=0 \tag{6}$$

An iteration scheme can be applied to Eqs. (5) and (6) for the values $U=(u,v)^T$ associated with the sides of a computational cell; the resulting algorithm is

$$U^{(\ell+1)}_{\cdot}=U^{(\ell)}_{\cdot}+\omega B^T(B\cdot B^T)^{-1}\begin{bmatrix}R_1(U^{(\ell)}_{\cdot})\\ R_2(U^{(\ell)}_{\cdot})\end{bmatrix} \tag{7}$$

where $U^{(\ell)}_{\cdot}$ is the approximation to $U_{\cdot}$ at the ℓth iteration,

$$B\equiv\begin{bmatrix}\Lambda_{\cdot}I, & -\Lambda_{\cdot}I, & C, & -C\\ I, & I, & -I, & -I\end{bmatrix}, \quad C=\begin{bmatrix}0 & 1\\ -1 & 0\end{bmatrix} \tag{8}$$

I is the 2×2 identity matrix, $\Lambda_{\cdot}$ the aspect ratio $\Delta y_k/\Delta x_j$ of each cell, and $\omega(=1.7)$ an extrapolation parameter whose

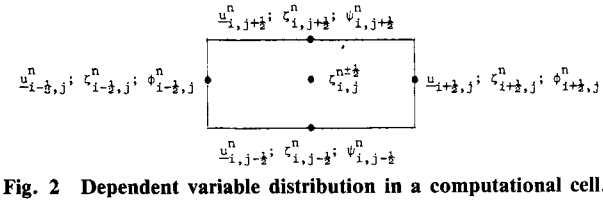

Fig. 2 Dependent variable distribution in a computational cell.

value is determined by numerical experiments. $R_1(U^{(\ell)})$ and $R_2(U^{(\ell)})$ are residuals defined by

$$R_1(U^{(\ell)}) \equiv \delta_x U^{(\ell)} + C\delta_y U^{(\ell)} - (0,\zeta)^T \tag{9a}$$

$$R_2(U^{(\ell)}) \equiv \mu_x U^{(\ell)} - \mu_y U^{(\ell)} \tag{9b}$$

Thus, Eq. (7) is analogous to an SOR-type iterative technique. At cells adjacent to the boundaries the matrix B is altered to account for the known velocity values at the edges of the bounding cells.

In the solution procedure the flow domain is divided into two regions: the region above the bounding flat plate and cavity, that is, the top region, and the cavity region itself. The coupling of the two regions in an overall solution solver will be described in Sec. IIC. For the present it will suffice to specify the boundary conditions in each region.

In the top region, the inflow u velocity is specified and is determined from the Blasius solution to the streamwise momentum equation for a given inflow boundary-layer thickness. This u velocity boundary condition is time independent. Along the flat plate, the v velocity is set to zero, and along the top of the computational domain, the nondimensional freestream velocity u is set to unity. Both of these boundary conditions are also time independent. Finally, at the outflow boundary, a time dependent flux condition for the v velocity is used, that is,

$$v^n_{M,k} = v^{n-1}_{M,k} - \Delta t\,(u^{n-1}_{M,j}\nabla_x v^{n-1}_{M,j} - v^{n-1}_{M,j}\nabla_x u^{n-1}_{M,j}) \tag{10}$$

where $j+\frac{1}{2} = M$ is the location of the outflow edge of the downstream boundary cells. Note that, in Eq. (10), the continuity equation (1) has been utilized.

The problem of specifying numerical outflow boundary conditions is important, difficult, and not yet totally solved. The most complete treatment of this problem, though mainly for inviscid flows and using linear analysis, is that of Oliger and Sundstrom.[12] The results of their study suggest that, for the two-dimensional flow of a viscous incompressible flow, two outflow boundary conditions are required. One of these should involve u and the other ζ. Numerical experiments with various conditions for u, as well as for v in both channel and boundary-layer flows have been conducted using this velocity-vorticity algorithm. These experiments have included: 1) specification of u; 2) specification of $\partial u/\partial x = 0$; 3) specification of v; and 4) $dv/dt = 0$. In all cases, the calculations were stable. Depending on which of these conditions were used, spurious numerical boundary layers, with different thicknesses, formed at the outflow boundary. Additional tests with perturbations introduced upstream were also performed. These perturbations propagated downstream as Tollmien-Schlichting waves and were partially reflected from the outflow boundary. The smallest outflow boundary layers and least reflection occurred when $dv/dt = 0$ was used as the outflow boundary condition. This is not surprising once it is realized that $dv/dt = 0$ is the finite amplitude, inviscid Rayleigh stability equation.[13] The use of this boundary condition, at least for moderate and high Reynolds numbers, permits flow perturbations to propagate "cleanly" through the outflow boundary. Of course, similar arguments can be used for $d\zeta/dt$ as an outflow boundary condition for the vorticity.

In the cavity region, the specification of the boundary conditions is straightforward. Along the solid boundaries of the cavity, the normal velocity components are specified. All these velocities are zero and are time independent. Along the interface with the top region of the computational domain, all velocities are required to be continuous. The details of the solution sequence at the interface will be described in Sec. IIC.

B. Vorticity Difference Equations and Solver

The difference approximations to Eq. (3) and the auxiliary averaging conditions needed in the solution procedure are given by[10]

$$(\delta_t + \hat{u}^n_{\cdot}\delta_x + \hat{v}^n_{\cdot}\delta_y)\zeta^n_{\cdot} = (1/R)(\delta_x\phi^n_{\cdot} + \delta_y\psi^n_{\cdot}) \tag{11}$$

with

$$\mu_t\zeta^n_{\cdot} = \mu_x\zeta^n_{\cdot} = \mu_y\zeta^n_{\cdot} \tag{12a}$$

$$\delta_x\zeta^n_{\cdot} = (\mu_x - \tfrac{1}{2}\Delta x_j q_x\delta_x)\phi^n_{\cdot} \tag{12b}$$

$$\delta_y\zeta^n_{\cdot} = (\mu_y - \tfrac{1}{2}\Delta y_k q_y\delta_y)\psi^n_{\cdot} \tag{12c}$$

where

$$\hat{u}^n_{\cdot} = \mu_x u^n_{\cdot}, \qquad \hat{v}^n_{\cdot} = \mu_y v^n_{\cdot}$$

$$q_x = q(\theta_x) = \coth\theta_x - \theta_x^{-1}, \qquad q_y = q(\theta_y) = \coth\theta_y - \theta_y^{-1}$$

$$\theta_x = u_{\cdot}\Delta x_j R/2, \qquad \theta_y = v_{\cdot}\Delta y_k R/2 \tag{12d}$$

As shown in Ref. 10, this system of equations, and the corresponding ADI approximations, can be solved by repeated use of a tridiagonal system of equations. For example, in the x direction the ζ^n variables associated with the sides of each cell are determined from

$$\begin{aligned}&\tfrac{1}{2}[(1-q_x)(1+\lambda_x\hat{u}^n_{\cdot}) - K_x]\zeta^n_{j+1,k} + \tfrac{1}{2}[(1+q_x)\\ &\times(1-\lambda_x\hat{u}^n_{\cdot}) - K_x]\zeta^n_{j-1,k} + [1+\lambda_x\hat{u}^n_{\cdot}q_x + K_x]\zeta^n_{j,k}\\ &= (1-q_x)g^n_{j+\frac{1}{2},k} + (1+q_x)g^n_{j-\frac{1}{2},k}\end{aligned} \tag{13}$$

where $\lambda_x = \Delta t/\Delta x_j$, $K_x = 2\Delta t/R\Delta x^2$, and the function g^n is described in Ref. 10. Note that the index $j = 1,2,\ldots,M-1$ varies over the range of cells in the x direction and that at each cell the coefficient values differ due to the dependence on grid size. The corresponding function $\phi^n_{\cdot}$ can be obtained from the vorticity values obtained in Eq. (13) by solving

$$\begin{aligned}\phi^n_{\cdot} = (R/4)\{&[(q_x-1)(1+\lambda_x\hat{u}^n_{\cdot}) + K_x]\zeta^n_{j+1,k}\\ &+ 2[q_x + \lambda_x\hat{u}^n_{\cdot}]\zeta^n_{j,k} + [(q_x+1)(1-\lambda_x\hat{u}^n_{\cdot}) - K_x]\zeta^n_{j-1,k}\\ &+ 2(1-q_x)g^n_{j+\frac{1}{2},k} - 2(1+q_x)g^n_{j-\frac{1}{2},k}\}\end{aligned} \tag{14}$$

With the solution of Eqs. (13) and (14), the solution set (ζ^n,ϕ^n) is known throughout the field; and with the solution of a completely analogous set of equations for the y direction, the solution set (ζ^n,ψ^n) will be known throughout the field. Once the variables (ζ^n,ϕ^n,ψ^n) are known at time level n, it is a simple step to directly impose either Eq. (11) or Eq. (12a) and obtain $\zeta^{n+\frac{1}{2}}_{\cdot}$ for the entire flowfield.

The remaining issue to be addressed is the choice of boundary conditions for the vorticity. Due to the tridiagonal formulation, it is not necessary in the vorticity solver to solve the equations in the top and cavity region separately, but to simply solve for the vorticity edge values by successive sweeps over the range of x and y values. Thus, in the x direction the sweep goes from the inflow boundary to the outflow boundary, and in the y direction from the flat plate or bottom of the cavity to the top of the computational domain. At the inflow boundary, the vorticity values are determined from the Blasius solution and are held fixed for all time. Along the flat plate and cavity solid boundaries, the vorticity is determined from second-order accurate one-sided difference approximation to the appropriate nonzero velocity derivative. Finally, along the top and outflow boundaries, vorticity flux conditions are applied. For example, the flux

condition applied at the outflow boundary, based on the argument of the previous section for the v velocity, is given by

$$\zeta^n_{M,k} = -\zeta^n_{M-1,k} + 2.0\zeta^{n-\frac{1}{2}}_{j} - \Delta t(\hat{u}^n_j \nabla_x \zeta^{n-\frac{1}{2}}_j + \hat{v}^n_j \nabla_y \zeta^{n-\frac{1}{2}}_j) \quad (15)$$

where $j = M - \frac{1}{2}$, k is the center of an outflow boundary cell. A completely analogous equation is used for determining the vorticity boundary values at the freestream boundary at the top of the computational domain.

C. Solution Procedure

The time-dependent solution for flow over the embedded cavity was obtained by first solving the equations for the flow over a flat plate and then using the flat plate solution field as initial conditions for the flow over an embedded cavity. The computational domain for the flat plate case was the same as the corresponding embedded cavity case except that the top of the cavity was replaced by a solid surface. All grid spacings in both cases were the same.

First, a description of the solution procedure for the flat plate case will be given. In all test cases presented, the initial values used throughout the flow domain were the appropriately averaged inflow Blasius velocity and vorticity fields. This initial set of field values is in error since it does not account for the boundary-layer growth in the streamwise direction and, even if boundary-layer growth were accounted for, the Blasius solution is not a solution to the full Navier-Stokes equations.

The solution procedure begins by entering the velocity solver, described in Sec. IIA, and iterating the solution set obtained from Eq. (7) until the convergence criteria

$$\max R_1(U^{(m)}_j), R_2(U^{(m)}_j) \le \min_{j,k}(\Delta x^2_j, \Delta y^2_k) \quad (16)$$

are met. When these criteria are met, the velocity values at time level n are known. From these velocity values, the requisite vorticity boundary values at time level n are determined using second-order accurate one-sided differences.

With the velocity field at time level n known, the vorticity field at time level n is required. As outlined in Sec. IIB, the solution procedure is a straightforward implementation of Eqs. (11-13), and the corresponding equations for the y direction, using the prescribed vorticity boundary conditions.[10] Once the vorticity values and their derivatives at the edges of the computational cells and at time level n are known, it is necessary to obtain the vorticity values associated with the center of each cell at time level $n+\frac{1}{2}$. This is done by solving the vorticity transport equation [Eq. (11)], or implementing the averaging condition equation [Eq. (12a)]. The solution procedure then continues onto the velocity solver with the vorticity values $\zeta^{n+\frac{1}{2}}_j$ as new input forcing functions.

The entire solution sequence continues until the number of iterations in the velocity solver falls to $m \le 3$, and the velocity and vorticity L_2 norms, that is, the energy and enstrophy, become time independent. A schematic representation of the solution sequence is shown in Fig. 3.

With the establishment of the flat plate solution, the computed velocity and vorticity values are used as input in the embedded cavity problem. The cavity domain is initially filled with zero values for both the velocity and vorticity.

In the velocity solver a two-step procedure is used: first, the cavity field is swept and the common velocity values at the interface between the cavity domain and top domain are equated; second, the top domain is swept using the boundary conditions and interface velocity values. The maximum residuals from both the cavity and top are compared with the convergence criteria, Eq. (16). The process is repeated through both the cavity and top computational domains until the convergence criteria are met. Once this occurs, the velocity field for the entire domain is known at time level n; and, in addition, the vorticity values along the solid boundaries are also known at time level n.

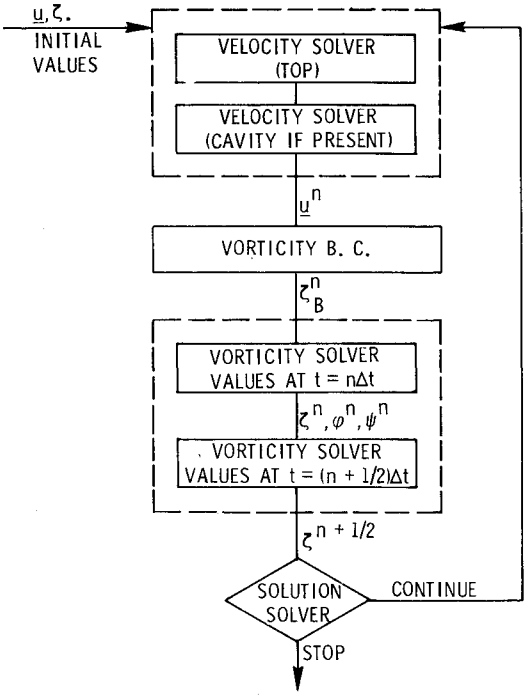

Fig. 3 Schematic of solution procedure.

The vorticity solution sequence is not altered by the presence of the cavity. The solution values are determined by sequential sweeps in both the streamwise and transverse directions. When the sweep is in the x direction, it is either from the inflow boundary to the outflow boundary in the top or from the left wall to the right wall in the cavity. When the sweep is in the y direction, it is either from the flat plate to the top of the computational domain or from the bottom of the cavity to the top of the computational domain. This procedure yields ζ^n, ϕ^n, and ψ^n values for the entire domain. Finally, the $\zeta^{n+\frac{1}{2}}$ vorticity values at the center of the computational cells for both the top and cavity domains are determined from either Eq. (11) or (12a).

From the results of the computations, it appears that even with the embedded cavities the flow does reach a state of dynamic equilibrium. Thus, the computational procedure continues for the flow over an embedded cavity until the termination criteria of $m \le 3$ and time independent L_2 norms are met.

III. Results and Discussion

The results presented were compiled from four test cases. All cavities were square and ranged from 0.25 to 1.00 boundary-layer thicknesses deep. In order to establish the relevant base parameters from which the calculations could be run, the experimental study of Ref. 6 was used as a guide. This was done to insure that over the range of parameters studied the flow in the vicinity of the cavity could be characterized as laminar separating flow and that within this computational range the flow neither became transitional nor turbulent. The reference boundary-layer thickness was determined from a Blasius solution of the streamwise momentum equation at a dimensional distance of $x = 80$ cm from the leading edge of the flat plate and a corresponding freestream velocity of 120 cm/s. The boundary-layer thickness was $\delta_0 = 1.68$ cm and the reference Reynolds number, $R = U_\infty \delta_0 / \nu$, was 1188.

The flow domain was discretized into a nonuniform set of Cartesian grid cells in the top boundary-layer region and a set of uniform grid cells in the cavity. The minimum and maximum nondimensional grid cell sizes ranged from 0.0125 to 0.8, respectively. The largest were placed away from regions of dynamic significance. The grid cell distribution in the cavity ranged from 10×10 cells in the smallest cavity to 40×40 cells in the largest cavity. In the case of the smallest cavity, the number of grid cells in the cavity was increased to 20×20 to insure the accuracy of the results with the coarser grid. In the top region, the number of grid cells in the vertical direction was held fixed at 40, and the number of grid cells in the streamwise direction ranged from 70 in the small cavity case to 90 in the large cavity case. In all cases the ratio of lengths in a given direction in adjacent cells never exceeded 2. The freestream boundary was located approximately 5 boundary-layer thicknesses above the flat plate; and the inflow and outflow boundaries were placed approximately 2.5 and 5 boundary-layer thicknesses upstream and downstream of the cavity, respectively. In all cases pressure contour plots were used to confirm that none of the computational boundaries interferes with the physical results in the vicinity of the cavity.

Figure 4 shows stream function contours in the vicinity of the cavity. It must be noted that, in this figure and subsequent figures where the cavities are sketched, the physical size of the cavities differ; however, for presentation purposes, the cavity sizes in the figures have been normalized. In all the contour plots presented, the dashed lines represent contours with negative values and solid lines represent contours with positive values. In addition, it is important to recognize that, in all the contour plots shown, no smoothing of the contour lines was attempted. Even though this is the reason for the jaggedness found in some of the contour plots, it was felt that this is a truer representation of the computed results. The values for the stream function contours shown, as well as for the vorticity contours that follow, were chosen to best represent the boundary-layer flow in the vicinity of the cavity and the recirculation zone within the cavity. Even though this precluded the representation of the corner vortices at the bottom of the cavities, it is not a reflection of either poor numerical resolution or degradation of accuracy in these regions. As can be seen, a strong recirculation region characterizes the cavity flow over most of the cavity. This causes the flow in the vicinity of the interface with the outer boundary flow to be accelerated locally; that is, a favorable pressure gradient is induced locally by the presence of the cavity. This effect is depicted by the convex curvature of the $\Psi = 10^{-4}$ streamline at the mouth of the cavity. This slightly nonzero value was chosen

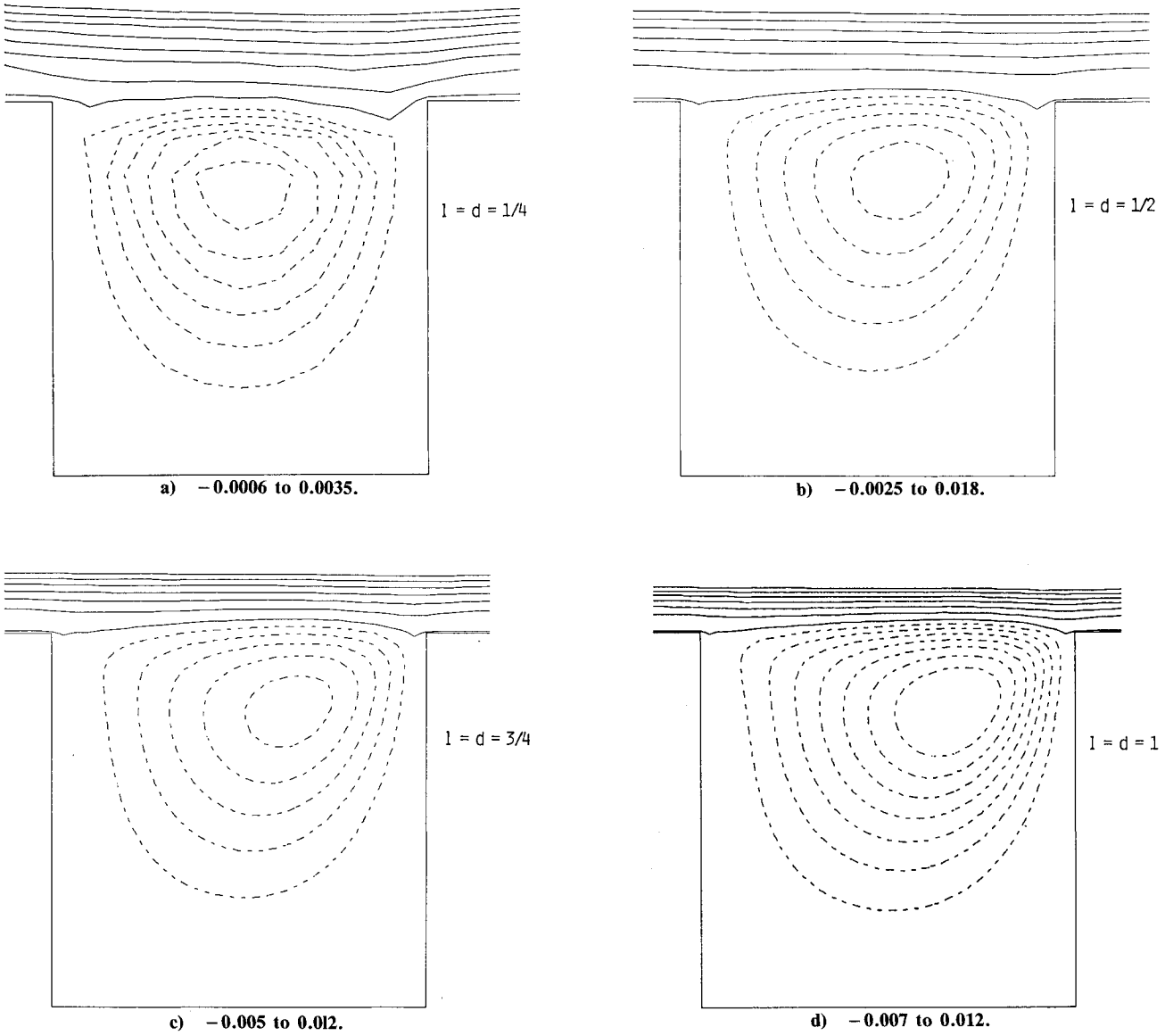

Fig. 4 Stream function contours; contour levels.

for this stream function contour, rather than the bounding streamline value of 0.0, to better illustrate the alteration of the boundary-layer flow both upstream and downstream of the cavity. Note, also, that this $\Psi = 10^{-4}$ streamline is located at differing distances from the flat plate bounding surface. This is due to the fact that, as indicated earlier, the different physically sized cavities have been normalized for presentation purposes. As the cavities deepen, although they remain square, the recirculation region begins to be skewed to the downstream side of the cavity. This increases the curvature of the streamline pattern in the vicinity of the cavity; thus causing a more favorable local pressure gradient and a stronger local flow acceleration. It should be pointed out that in the Reynolds number and cavity sizes studied, no laminar flow instabilities arose in this bounding shear layer. Since this was a time-dependent numerical study incorporating the full form of the vorticity transport equation, any interfacial instabilities, either spatial or temporal, would be easily detected in the stream function contour plots. An examination of these plots, or the vorticity contour plots to be presented next, showed no indication of interfacial instabilities. This observation is in agreement with Ref. 4, where no laminar oscillations occurred below a cavity Reynolds number, $U_\infty d/\nu$, of 2400. In the present study, the maximum cavity Reynolds number is approximately 1200.

The isovorticity contours in Fig. 5 show that, as the cavity size increases, the vortex in the cavity is indeed skewed to the downstream side of the cavity. This downstream shift causes a thickening of the shear layer on this side of the cavity. Note that this asymmetry of vorticity in the vortical recirculation region must also cause a corresponding increase of vorticity, of opposite sign, in the immediate vicinity of the downstream wall of the cavity as well. A consequence of this is the strengthening of the relatively weak vortex region present in the lower right-hand corner of the cavity. This is due to the fact that fluid is accelerated downstream by the action of the two counterrotating vortical regions at the top of the cavity and this accelerated fluid causes the strengthening of the rotational motion at the bottom of the cavity. Note that the stream function contours did not indicate the presence of the recirculation regions at the bottom of the cavities. This was due to the fact that the vorticity is a more sensitive measure of such flow dynamics and to include such motion into a streamline representation would have required an unnecessary significant increase in the number of streamline contours. Finally, it can be concluded that in the temporal development of the embedded cavity flow, the vortex in the lower downstream corner of the cavity must be developed before the vortex in the lower upstream corner of the cavity. This leads to the speculation that if the downstream vortex is

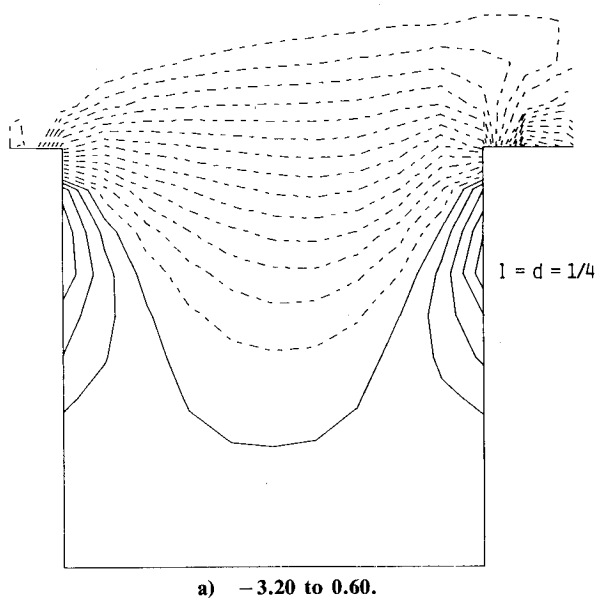

a) −3.20 to 0.60.

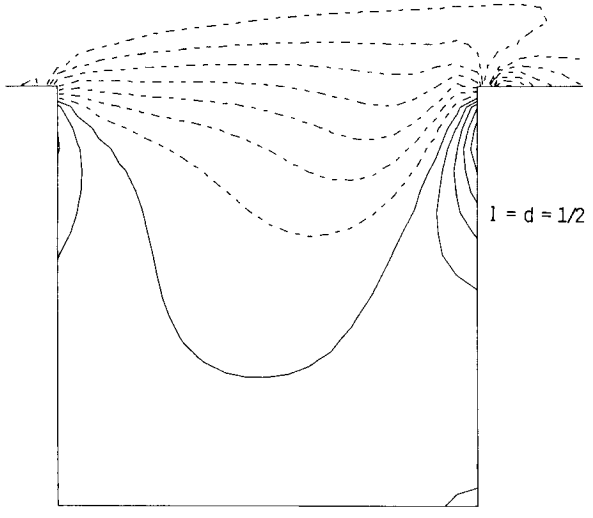

b) −2.80 to 1.00.

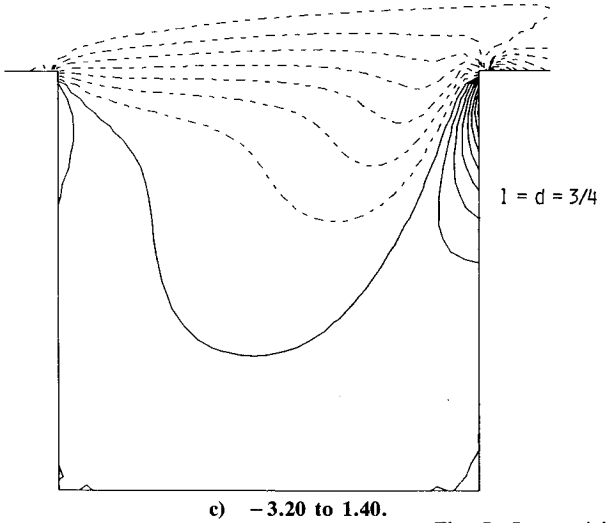

c) −3.20 to 1.40.

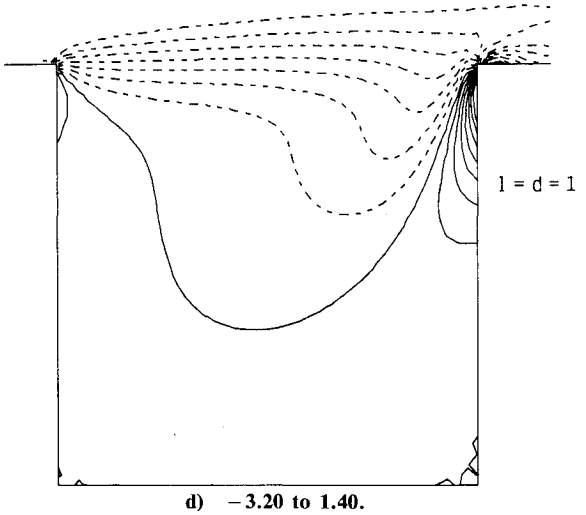

d) −3.20 to 1.40.

Fig. 5 Iso-vorticity contours; contour levels.

precluded from forming, by either flow suction or some other means, then the upstream vortex may also be inhibited.

One of the main objectives of the present study was to examine the effects of the embedded cavity on total drag. In the absence of the cavity the drag is due solely to skin friction; with the cavity, the effects of pressure drag on the vertical walls of the cavity must be accounted for in addition to friction drag. A comparison of integrated C_D/C_F between the flat plate with cavity and the flat plate is shown in Fig. 6 as a function of the nondimensional streamwise coordinate x. Upstream of the cavity there is very little difference between the two cases, although there is a slight increase near the upstream corner of the cavity in all cases. Along the upstream vertical wall, the pressure thrust is such as to cause a local drag reduction; and along the downstream vertical wall, the pressure drag is such as to cause a local drag increase. Note that pressure drag increase on the downstream vertical wall is larger than the pressure drag decrease on the upstream vertical wall. In addition, the frictional drag on the bottom of the cavity is significantly lower than the reference frictional drag on the corresponding flat plate in the absence of the cavity. This, of course, is due to the insignificant induced motion on the bottom of the cavity. In fact, if these were the only additional induced forces due to the presence of the cavity, the net drag reduction would be approximately 3, 5, 9, and 7%, respectively, for the range of shallow to deep cavities studied. Unfortunately, there is another dynamic process involved which causes an additional increase in drag. Even in the laminar flow case studied here there are stress relaxation effects present in the flow. As can be seen in Fig. 6, these frictional forces cause the total drag to eventually relax back to the flat plate boundary-layer case. Thus, in the present study the embedded cavities do not appreciably alter the drag characteristics of the flow. This is in agreement with the laminar behavior of rough walls as documented in Ref. 14.

Even in light of the benign effect of the embedded cavities, it is of interest to analyze in some detail the various contributing forces to the total drag. In Fig. 7 are depicted the variations of C_P on the upstream and downstream vertical walls of the cavity as well as on the bottom of the cavity. As is shown, only near the top of the cavity at the upstream corner do pressure forces act to reduce the overall drag. In the remaining portions of the vertical walls, pressure forces add to the net drag. It is also of interest to note in this figure that the pressure is relatively uniform over a large portion of the cavity and that any significant pressure thrust or pressure drag occurs in the upper portions of the cavity near the corners. It is difficult to compare these results with previous experimental studies, even those of Ref. 6, since the square cavities studied in this work are much shallower. For example, as is seen in Fig. 7, the value of C_P decreases on the upstream wall of the cavity as the corner is approached. This reflects the fact that, in such a stable laminar flow,

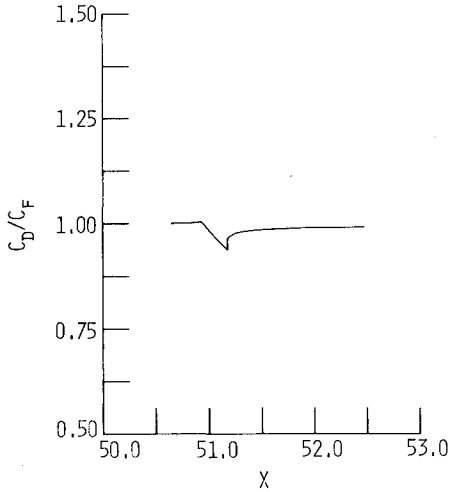

a) $\ell = d = \frac{1}{4}$.

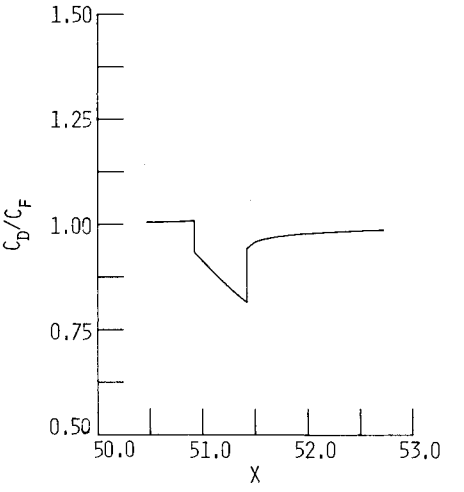

b) $\ell = d = \frac{1}{2}$.

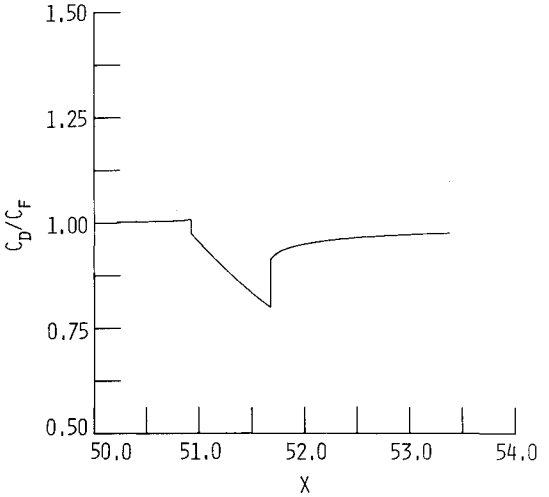

c) $\ell = d = \frac{3}{4}$.

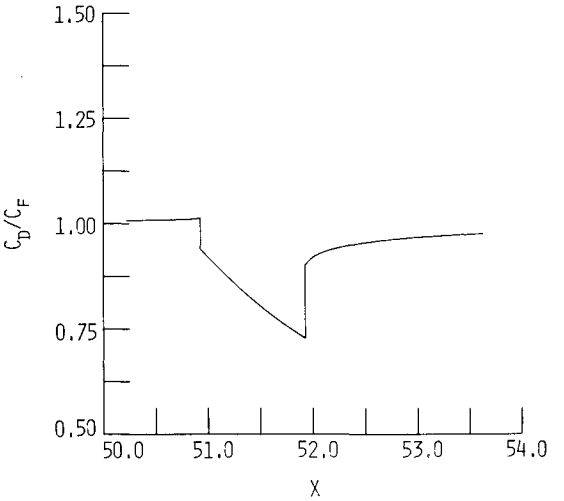

d) $\ell = d = 1$.

Fig. 6 C_D/C_F as a function of streamwise distance x.

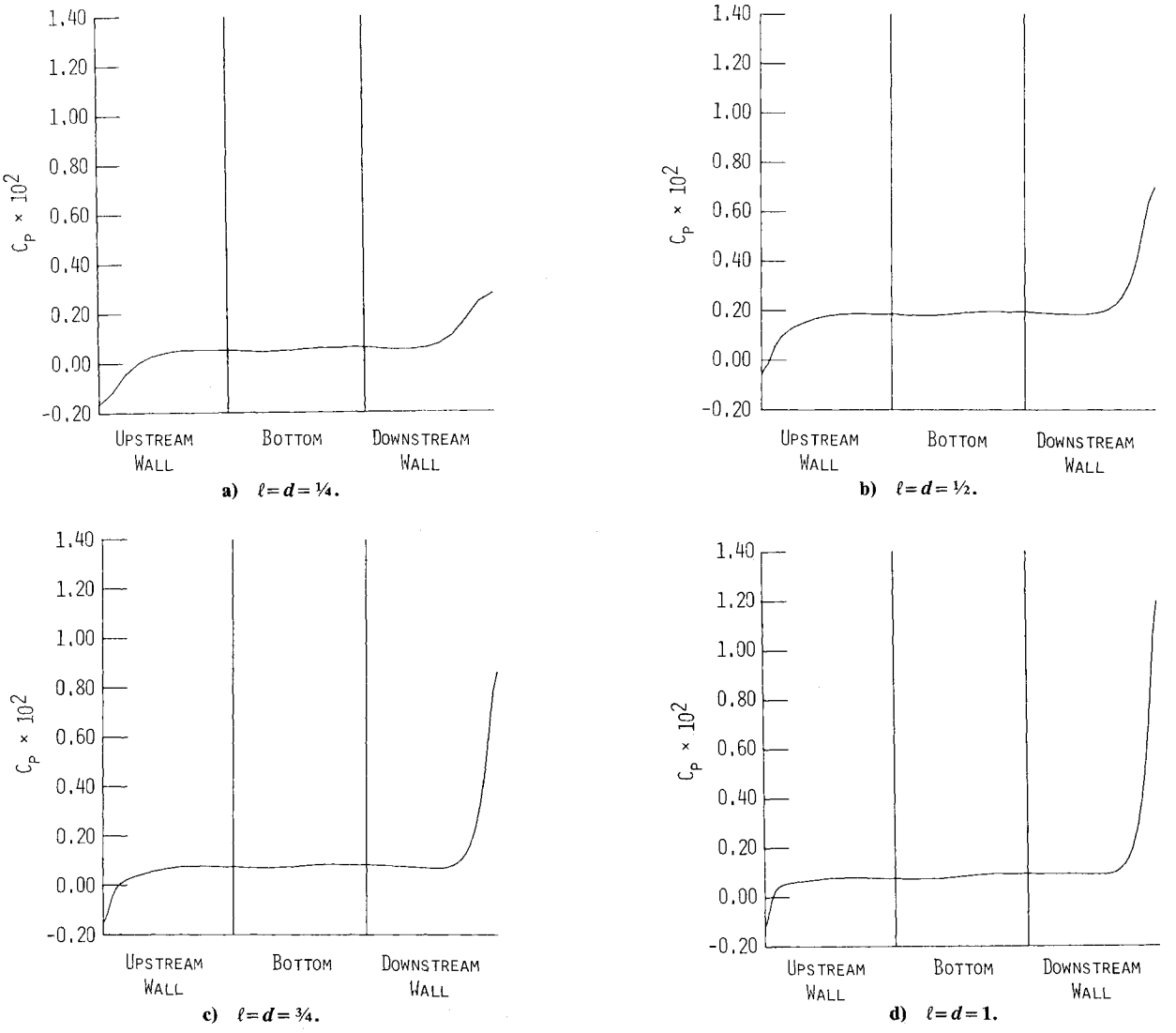

Fig. 7 C_P along walls and floor of cavity.

separation occurs near the corner of the cavity. An examination of the results for C_P presented in Ref. 6 (see their Fig. 5) for square cavities, which are approximately two boundary-layer thicknesses deep and have a cavity Reynolds number of 2648, reveals no such separation. Thus, either the resolution provided by the pressure probes within the cavity was insufficient, or the unsteadiness of the bounding shear layer precluded the identification of any such separation region.

Finally, it is necessary to examine the remaining contributor to the total drag, that is, the drag due to the stress overshoots upstream and downstream of the cavity. In Fig. 8 the variation of the wall shear stress, $\tau_w = (1/R)(\partial u/\partial y)_w$, with downstream location is shown. Recall that the downstream boundary of the computational domain extends beyond the region shown in this figure, but for presentation purposes this region is not shown. However, the stress distributions in all cases relaxed back to their flat plate values, and since the wall shear stress is a relatively sensitive quantity, this fact provides further confirmation that the downstream boundary location did not affect the computed results. The stress overshoot regions, relative to the flat plate case, are clearly depicted in the figure. Note that the flat plate wall shear is indicated by the dashed line which, of course, is a decreasing function of the streamwise distance x. In all cases, the magnitudes of the overshoots are quite similar; however, the relaxation distances tend to increase with the size of the cavity. This suggests that a maximum separation distance exists, beyond which the cavities act independently and no net drag reduction occurs. If the cavities are placed within the relaxation distance it may be possible to effectively couple the sequential cavities and achieve some net drag reduction. This type of placement is further indicated by the drag due to the stress relaxation. For example, in the four cases examined, the drag increase due to the stress overshoots is about 35% of the frictional drag decrease due to the presence of the cavity. Thus, if some means of minimizing the overshoots could be found, either by optimal spacing of sequential cavities or optimal design of the cavities themselves, then some net drag reduction might be realized.

Table 1 summarizes the component drag contributions from the pressure forces and frictional forces. In all cases the comparisons are made up to the end of the stress relaxation region downstream of the cavity. As is shown, the net reduction in drag, relative to the flat plate case, is insignificant for the cases studied in this work. Nevertheless, in the deepest cavity case, the reduction, even though small, is less than in the $d = 1/2$ and $d = 3/4$ cases. Whether this is the beginning of a trend toward increased drag for deeper cavities is not clear, and must, for the time being, remain as a subject for future study. However, as the cavity depth increases, the corresponding Reynolds number approaches the critical value of 2400 alluded to earlier, and the flow in the

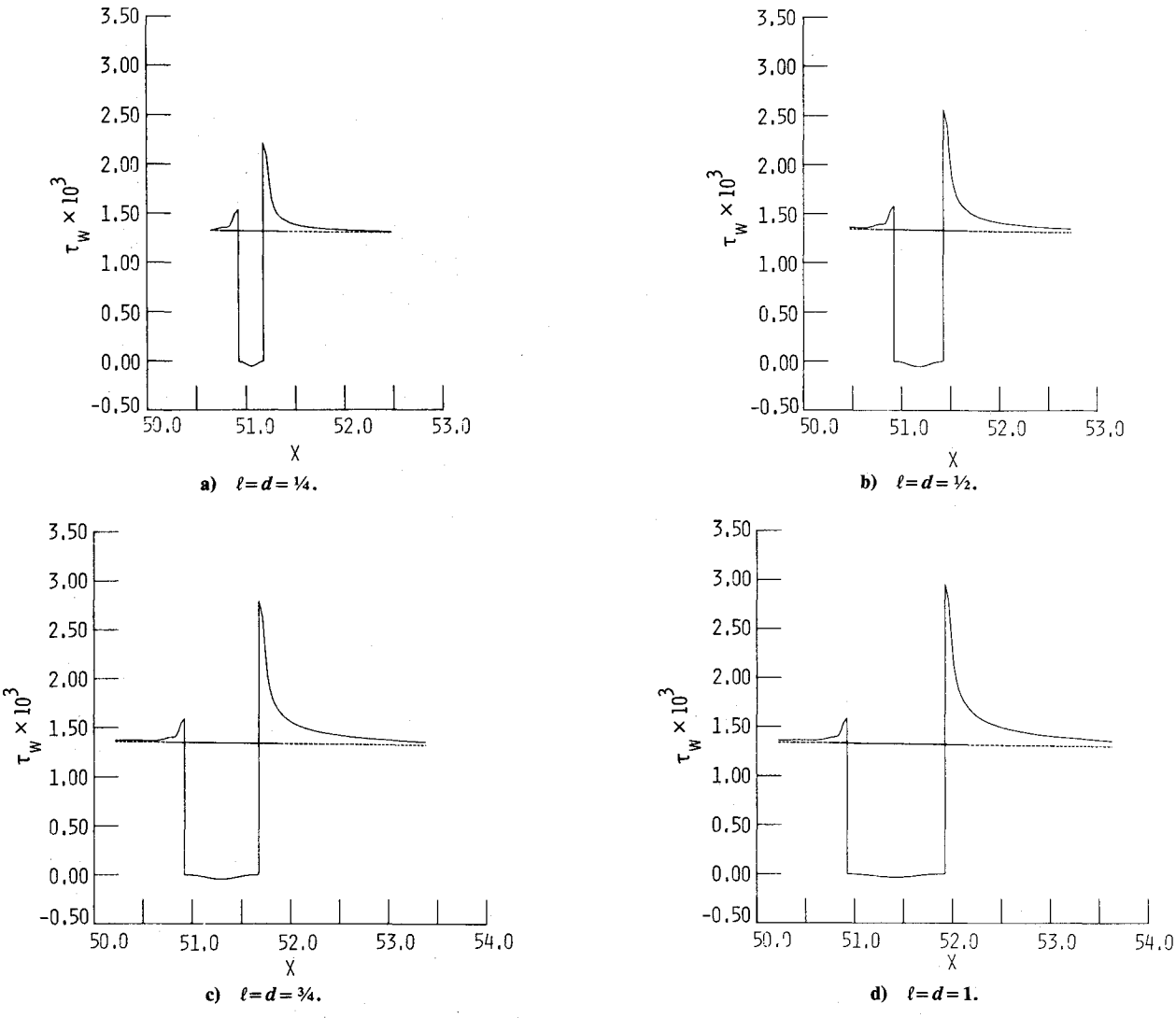

a) $\ell = d = 1/4$. b) $\ell = d = 1/2$. c) $\ell = d = 3/4$. d) $\ell = d = 1$.

Fig. 8 Wall shear stress as a function of streamwise distance x; flat plate reference case - - -.

Table 1 Distribution of drag forces and percent drag reduction

Cavity size	Pressure drag ($\times 10^{-4}$)	Differential friction drag[a] ($\times 10^{-4}$)	Total differential drag[b] ($\times 10^{-4}$)	Percent reduction[c]
$\ell = d = 1/4$	1.4	−2.0	−0.6	−0.9
$\ell = d = 1/2$	3.3	−4.2	−0.9	−1.3
$\ell = d = 3/4$	4.9	−6.8	−1.9	−2.4
$\ell = d = 1$	7.5	−8.7	−1.2	−1.5

[a]Frictional drag with cavity minus frictional drag without cavity. [b]Pressure drag plus differential frictional drag. [c]Total differential drag divided by frictional drag on flat plate.

separated shear layer becomes unsteady. This could cause an increase in the drag due to the additional momentum exchange between the boundary-layer flow and the flow in the cavity. Nevertheless, it can simply be stated that there is essentially no change in drag between the laminar flat plate case and the embedded cavity cases studied.

Finally, the fact that the flow in the vicinity of the cavity has a smaller momentum thickness than that of the flow on a flat plate suggests that a cavity may have a positive effect on a separating flow. The usual physical description of separation is that an adverse pressure gradient causes the deceleration of the low momentum flow near the surface. The results in this paper show that the cavity creates, in effect, a locally favorable pressure gradient, and since this is a local effect, it can be assumed that, even if the cavity were embedded in a boundary-layer flow with an adverse pressure gradient, the net local effect would be to produce a less adverse pressure gradient field in the vicinity of the cavity. It, therefore, appears that the introduction of a cavity at, or just forward of, the separation point on a body might shift the separation point downstream. Such a conjecture is substantiated by the results in Ref. 15, where circumferential grooves were used to delay separation and reduce drag on an axisymmetric bluff body. The detailed flow structure about a cavity placed in the vicinity of a separation point can be studied by the method described in this paper, and initial calculations on such flows are in progress.

IV. Conclusions

From the results presented in the preceding section, a clear picture of the flow in the vicinity of the cavity emerges. The presence of the cavity causes an upstream as well as downstream modification of the flow, as was seen from the variation of wall shear stress with position in Fig. 8. From these results, it can be seen that, in all cases, the upstream influence extends for a distance equal to about 0.25 of a boundary-layer thickness. Downstream of the cavity the region of cavity influence increases, with increasing cavity size. The length of this region changes from about 1 boundary-layer thickness for the smallest cavity to about

1.75 boundary-layer thicknesses for the largest cavity. Upstream of the cavity there is, effectively, a favorable pressure gradient; the boundary-layer thickness decreases and the shear stress increases. The flow accelerates across the cavity and, on the downstream edge of the cavity, the shear stress is very high, reaching approximately twice that of the zero pressure gradient Blasius boundary layer. Thus, for the range of cavity sizes studied, it can be concluded that cavities which are approximately 2-3 boundary-layer thicknesses apart can be treated as if they were isolated. An interesting question arises as to what the flow characteristics are for closely spaced cavities, those separated by a boundary-layer thickness or less.

Finally, as mentioned previously, the results of this study can be extrapolated to suggest that the placement of a cavity in the vicinity of a separation point can delay separation.

Acknowledgment

The authors would like to thank Mr. Peter Spence of ICASE for his expert utilization of the various computer graphics subroutines. The work of the second author was supported in part under contract NASI-17130 at ICASE.

References

[1]Walsh, M. J., "Optimization and Application of Riblets for Turbulent Drag Reduction," AIAA Paper 84-0347, Jan. 1984.

[2]Roshko, A., "Some Measurements of Flow in a Rectangular Cutout," NACA TM-3488, Aug. 1955.

[3]Tani, S., Suchi, M., and Komodo, M., "Experimental Investigation of Flow Separation Associated with a Step or a Groove," Aeronautical Research Institute, University of Tokyo, Rept. 364, April 1961.

[4]Reihman, T. C. and Sabersky, R. H., "Laminar Flow Over Transverse Rectangular Cavities," *International Journal of Heat Mass Transfer*, Vol. 11, June 1968, pp. 1083-1085.

[5]Sarohia, V., "Experimental Investigation of Oscillations in Flows Over Shallow Cavities," *AIAA Journal*, Vol. 15, July 1977, pp. 984-991.

[6]Sinha, S. N., Gupta, A. K., and Oberai, M. M., "Laminar Separating Flow Over Backsteps and Cavities, Part II. Cavities," *AIAA Journal*, Vol. 20, March 1982, pp. 370-375.

[7]Rockwell, D. and Knisely, C., "The Organized Nature of Flow Impingement Upon a Corner," *Journal of Fluid Mechanics*, Vol. 93, Pt. 3, Aug. 1979, pp. 413-432.

[8]Borland, C. J., "Numerical Prediction of the Unsteady Flowfield in an Open Cavity, AIAA Paper 77-673, June 1977.

[9]Hankey, W. L. and Shang, J. S., "The Numerical Solution to Pressure Oscillations in an Open Cavity," AIAA Paper 79-0136, AIAA 17th Aerospace Sciences Meeting, New Orleans, Jan. 15-17, 1979.

[10]Gatski, T. B., Grosch, C. E., and Rose, M. E., "A Numerical Study of the Two-Dimensional Navier-Stokes Equations in Vorticity-Velocity Variables," *Journal of Computational Physics*, Vol. 98, No. 1, Oct. 1982, pp. 1-22.

[11]McInville, R. M., Gatski, T. B., and Hassan, H. A., "Embedded Shear Layer Computations for Increased Drag Reduction," AIAA Paper 84-0349, Jan. 1984.

[12]Oliger, J. and Sundstrom, A., "Theoretical and Practical Aspects of Some Initial Boundary Value Problem in Fluid Dynamics," *SIAM Journal of Applied Mathematics*, Vol. 35, No. 3, Nov. 1978, pp. 419-446.

[13]Drazin, P. G. and Howard, L. N., " Hydrodynamic Stability of Parallel Flow of Inviscid Fluid," *Advances in Applied Mechanics*, Vol. 9, Academic Press, New York, 1966, pp. 1-89.

[14]Mills, A. F. and Courtney, J. F., "Turbulent Boundary Layers on Rough Walls," AFOSR-TR-76-1098, March 1976.

[15]Howard, F. G., Goodman, W. T., and Walsh, M. J., "Axisymmetric Bluff-Body Drag Reduction Using Circumferential Grooves," AIAA Paper 83-1788, July 1983.